

A pressure-based method with AUSM-type fluxes for MHD flows at arbitrary Mach numbers

C. M. Xisto^{*,†,‡}, J. C. Páscoa[‡] and P. J. Oliveira[§]

Dep. de Eng. Electromecânica, Universidade da Beira Interior, R. Mq.s D Ávila e Bolama, 6201-001 Covilhã, Portugal

SUMMARY

In this paper, we propose an extension of a PISO method, previously developed to solve the Euler equations, and which is here extended to the ideal magnetohydrodynamic (MHD) equations. By following a pressure-based approach, we make use of the flexibility given by pressure equation for calculating flows at arbitrary Mach numbers. To handle MHD discontinuities, we have adapted the MHD-Advection Upstream Splitting Method for our pressure-based formulation. With the purpose of validation, four sets of test cases are presented and discussed. We start with the circularly polarized Alfvén waves that serves as a smooth flow validation. The second case is the 1-D Riemann problem that is calculated using both 1-D and 2-D formulation of the MHD equations. The third and fourth problems are the Orszag–Tang vortex and the supersonic low- β cylinder allowing validation of the method in complex 2-D MHD shock interaction. Copyright © 2013 John Wiley & Sons, Ltd.

Received 29 August 2012; Accepted 15 January 2013

KEY WORDS: finite volume; compressible flow; AUSM; PISO; MHD; all Mach

1. INTRODUCTION

Flows of electrically conducting fluids, subjected to magnetic fields, can be found both in nature and in applications built by man. If the physical properties and characteristics of the flow field are adequate, then the magnetohydrodynamics (MHD) equations provide a useful model to describe the physical behavior of such flows. In metallurgic industry, we can find applications where magnetic field is used to control the injection of melted iron; in this case, an incompressible formulation of the MHD equations should be applied. But MHD can also be used to describe the behavior of some plasma flows in the field of astrophysics; and in this case, a compressible formulation is required, and the ideal MHD equations are normally used. Another application is the modeling of magnetoplasdynamic (MPD) thrusters used for spacecraft propulsion [1].

To calculate such variety of MHD flows, two groups of algorithms have been developed. The first group comprises methods designed to deal with incompressible flow [2] and the second to calculate highly compressible MHD flows [3–7]. However, nowadays, a great number of numerical gas dynamics codes are able to solve the compressible Navier–Stokes equations at all Mach number regimes. Such algorithms are important because in the field of aerospace engineering, there is often a need to solve complex flow problems that involve a wide range of Mach numbers. This is also true for the special case of MHD flow in realistic MPD thruster geometries. It is known that these

*Correspondence to: C. M. Xisto, Dep. de Eng. Electromecânica, Universidade da Beira Interior, R. Mq.s D Ávila e Bolama, 6201-001 Covilhã, Portugal.

†E-mail: xisto@ubi.pt

‡CAST Research Unit

§CEFT Research Unit

devices can produce flows that range from the nearly incompressible to the hypersonic limit [8]. Despite these needs, there is still a lack of solvers capable of solving efficiently the compressible MHD equations for the whole range of Mach number regimes.

Several shock-capturing methods were developed for the numerical calculations of ideal MHD equations. Some of the first methods were based on the artificial viscosity technique [9, 10]. However, Falle [11] realized that such an approach does neither introduce upwind to all characteristic fields involved nor is it conservative, and, because of these deficiencies, it leads to inappropriate results in the calculation of some discontinuities.

A more complex set of methods incorporate the full seven-wave structure of the MHD equations and were introduced by various authors [3, 12, 13]. These methods account for all types of discontinuities in their formulation, and, therefore, they are the most accurate for shock wave calculations. When these characteristic-based methods were extended to the ideal MHD equations, they were already well established for the calculation of pure gas dynamics flows. Albeit this, their application to MHD flows was delayed, in particular because its extension to MHD was nontrivial; in fact, the structure of the MHD equation system is by far much more complex than the structure of the Euler equations. One of the most successful techniques was a MHD Godunov method used by Zachary and Collela [13]; another one was a total variation diminishing (TVD) Roe-type scheme introduced for MHD by Ryu and Jones [3].

In contrast with the pure characteristic-based methods, some methods replace the seven-wave structure by an approximation, taking into account only the maximal wave speed. This is still a valid upwind concept, but it is more dissipative; however, in some cases, can be advantageous in terms of robustness. One of such methods is the Lax–Friedrich’s TVD method that was extended to the MHD equations by Tóth and Odstreil [4]. Another method that uses a similar approach is the Harten–Lax–van Leer (HLL) method. Janhunen [14] extended the HLL method with a Roe solver for MHD. The HLL is very stable and guarantees the positivity of the thermodynamic variables in its formulation; however, it is quite dissipative, specially in contact discontinuities, the main reason being that it does not have a mechanism to recognize this kind of discontinuity. Linde [15] proposed a corrected formulation of the HLL solver to account for the contact discontinuity. Li [5] adapts the HLLC (‘C’ for contact discontinuity) method of Toro *et al.* [16] to MHD, and this new method already accounts for the contact discontinuity in its formulation. Miyoshi and Kusano [6] added two more intermediate states to the Riemann fan of the previous HLL solver and in this way developed a more accurate HLLD (‘D’ is for discontinuity) solver. Mignone [17] adapted this HLLD method for isothermal MHD.

Han *et al.* [18] presented a reformulation of the Advection Upstream Splitting Method by Pressure based Weight functions (AUSMPW) method [19] and M-AUSMPW+ method [20] for MHD. They have demonstrated that the base AUSMPW scheme was unstable for the calculation of discontinuities in some 1-D Riemann MHD problems. Because of that, they have included the effect of magnetic pressure in the calculation of the weighting functions. Like the aforementioned Lax–Friedrich’s TVD and HLL methods, this approach does not need to know the full structure of the MHD equations. This formulation is mainly based on the fast wave speed, and, because of that, the level of complexity of its implementation is not so high as in the original characteristic-based methods. At the same time, like all AUSM-based methods, it proves to be very accurate and stable for shock wave calculations.

A pressure-correction method for all Mach MHD equations was presented by van der Heul *et al.* [21]. This method is based on a nondimensional formulation of the MHD equations that is based on the Mach number. However, this formulation was only tested for a restricted number of test cases and requires a more complete level of validation.

A problem that arises in the numerical calculation of multidimensional MHD is satisfying the $\nabla \cdot \mathbf{B} = 0$ constraint. Brackbill and Barnes [22] have shown that even if this constraint is fully satisfied in the first time level, errors related to space and time discretization can result in a nonzero divergence of the magnetic field later in the calculation. Several methods were introduced to handle this question. One solution is the projection method originally mentioned by Brackbill and Barnes [22], which is similar to the projection methods developed for incompressible fluid dynamics solvers to ensure that $\nabla \cdot \mathbf{U} = 0$, as imposed by the continuity equation. Another technique is the constrained

transport method, proposed by Evans and Hawley [9], in connection with a finite difference discretization on a staggered grid that ensures that the solenoidal constraint is satisfied with machine precision accuracy. Tóth [23] adapted this constrained transport technique to finite volume methods that do not rely on the use of a staggered grid.

An alternative simpler approach would be the introduction of source terms proportional to $\nabla \cdot \mathbf{B}$ in the MHD equations as in the work of Powell *et al.* [24]. However, Janhunen [14] have tested this approach to low- β plasmas and noticed that the introduction of these nonconservative terms in the momentum and energy equations can lead to negative thermodynamic pressures. He suggested that the source terms should be removed from these equations and only keep a nonconservative formulation in the induction equation. An excellent review and comparison between all of the previous methods can be found in [23]. We have chosen a different approach that was proposed by Dedner *et al.* [25]. They have found a way of coupling the $\nabla \cdot \mathbf{B} = 0$ constraint with the induction equation by means of a scalar function through a gradient term. After solving a hyperbolic/parabolic equation for the new scalar function, the errors can be advected at a maximal speed and damped locally using a proper dissipative coefficient.

In the present paper, we present and discuss an arbitrary Mach number MHD solver on the basis of the PISO method, a well-known pressure-correction method. This new solver is an extension of a previous method, which we have devised for the Euler equations [26], to the compressible and ideal MHD equations.

In the next section, we present the governing equations, and in Section 3, the numerical method is described in detail, together with the algorithm that couples all the unknown variables involved. The special technique proposed by Dedner *et al.* [25] to remove the numerical errors arising from the lack of satisfaction of Gauss law for the magnetic field is also briefly described.

In Section 4, four different sets of test cases are considered for validation. The first comprises 1-D and 2-D circularly polarized Alfvén waves, with the purpose of validating our method for smooth flows at low Mach number ($Ma \approx 0.2$). The second set is a 1-D Riemann problem, which is tackled using the 1-D and the 2-D formulation of the MHD equations (obtained by rotating the flow domain). This test case will allow us to validate the algorithm for high Mach number flows possessing discontinuities in both velocity and magnetic fields. The third test case is the Orszag–Tang vortex, which is a standard 2-D case for MHD schemes, and we use this case to compare our results with those obtained with a density-based method. The final test case is the calculation of a low- β plasma flow over a perfectly conducting cylinder, where we can see the effect of plasma β and incoming velocity in the occurrence of exotic MHD discontinuities.

2. GOVERNING EQUATIONS

Magnetohydrodynamics is related to the interaction of a conducting moving fluid with one or more magnetic fields. This interaction can be described by the MHD equations, which couple the magnetic field, given by Maxwell equations, with the flow of a conducting fluid, ruled by the Euler equations. The MHD equations for a perfectly conducting fluid, written in a conservative form, are given by the following:

$$\frac{\partial \rho}{\partial t} + \nabla \cdot (\rho \mathbf{U}) = 0, \quad (1)$$

$$\frac{\partial \rho \mathbf{U}}{\partial t} + \nabla \cdot \left[\rho \mathbf{U} \mathbf{U} + \left(p + \frac{\mathbf{B} \cdot \mathbf{B}}{2} \right) \mathbf{I} - \mathbf{B} \mathbf{B} \right] = 0, \quad (2)$$

$$\frac{\partial \rho e}{\partial t} + \nabla \cdot \left[\left(\rho e + p + \frac{\mathbf{B} \cdot \mathbf{B}}{2} \right) \mathbf{U} - \mathbf{U} \cdot \mathbf{B} \mathbf{B} \right] = 0, \quad (3)$$

$$\frac{\partial \mathbf{B}}{\partial t} + \nabla \cdot (\mathbf{U} \mathbf{B} - \mathbf{B} \mathbf{U}) = 0, \quad (4)$$

with the magnetic field subjected to the following Gauss law:

$$\nabla \cdot \mathbf{B} = 0. \quad (5)$$

This system expresses the conservation of mass (1), momentum (2), total energy (3), and propagation of the magnetic field (4 and 5). We have chosen units such that the vacuum magnetic permeability (μ_0) becomes equal to unity. A global pressure can be defined by the sum of the mechanical and magnetic pressures as follows:

$$p_G = p + \frac{\mathbf{B} \cdot \mathbf{B}}{2}. \quad (6)$$

In the algorithm proposed here, the mechanical pressure, p , is calculated indirectly via an equation assembled using both the continuity (Equation (1)) and the momentum (Equation (2)) equations, following standard practices of pressure-correction algorithms. Temperature is a derived quantity and is obtained through an equation of state as follows:

$$T = \frac{1}{c_v} \left[e - \frac{1}{2} \left\{ \mathbf{U} \cdot \mathbf{U} + \frac{\mathbf{B} \cdot \mathbf{B}}{\rho} \right\} \right]. \quad (7)$$

3. NUMERICAL METHOD FOR MULTIDIMENSIONAL MAGNETOHYDRODYNAMICS

In the following subsections, we describe the method devised for solving the multidimensional MHD equations of the previous section. Firstly, we explain how the set of conservative fluxes are calculated using a modified version of the AUSM method especially developed for the MHD equations. Secondly, we briefly describe the numerical technique used to guarantee that the constraint given by $\nabla \cdot \mathbf{B} = 0$ is satisfied at all times. Finally, all the steps of the solution algorithm that couples the dependent variables are outlined and discussed in detail. We make use of the Open Field Operation and Manipulation package as a developer tool for our new code. The Open Field Operation and Manipulation code is an object-oriented numerical simulation toolkit for continuum mechanics, written in C++ language, released by Silicon Graphics International Corporation. The main advantage of this tool is that it is open source, thus allowing the user to modify the source code and take advantage of contributions from a worldwide community.

3.1. Conservative fluxes

The AUSMPW-MHD [18] technique allows us to calculate the set of conservative fluxes that are then assembled as the MHD system of discretized equations. For 3-D flow, exhibiting variations along the x -, y - and z -directions, the system of equations can be written in the following conservative form:

$$\frac{\partial \mathcal{H}}{\partial t} = \frac{\partial \mathcal{F}_x}{\partial x} + \frac{\partial \mathcal{F}_y}{\partial y} + \frac{\partial \mathcal{F}_z}{\partial z}, \quad (8)$$

where \mathcal{H} is the state vector for the conservative variables and $\mathcal{F}_{x,y,z}$ represents the flux vectors in each direction. These are given by the following:

$$\mathcal{H} = \begin{pmatrix} \rho \\ \rho U_x \\ \rho U_y \\ \rho U_z \\ \rho e \\ B_x \\ B_y \\ B_z \end{pmatrix}, \quad \mathcal{F}_x = \begin{pmatrix} \rho U_x \\ \rho U_x^2 + p_G - B_x^2 \\ \rho U_x U_y - B_x B_y \\ \rho U_x U_z - B_x B_z \\ (\rho e + p_G) U_x - B_x (B_x U_x + B_y U_y + B_z U_z) \\ 0 \\ B_y U_x - B_x U_y \\ B_z U_x - B_x U_z \end{pmatrix}, \quad (9)$$

with \mathcal{F}_y and \mathcal{F}_z obtained by permutation of indices. The global pressure and total energy are given by the following:

$$p_G = p + \frac{1}{2} (B_x^2 + B_y^2 + B_z^2), \quad (10)$$

$$e = \frac{1}{2} (U_x^2 + U_y^2 + U_z^2) + C_v T + \frac{1}{2\rho} (B_x^2 + B_y^2 + B_z^2). \quad (11)$$

Using the AUSM⁺ method of standard gas dynamics, we can calculate the flux function at any cell face (index f) as follows:

$$\mathcal{F}_f = a_f (\mathcal{M}_4^+ \phi_L + \mathcal{M}_4^- \phi_R) + (\mathcal{P}_5^+ P_L + \mathcal{P}_5^- P_R), \quad (12)$$

where a_f is the common speed of sound, $\phi = (\rho, \rho \mathbf{U}, \rho e)^T$ and $P = (0, p, 0)^T$. The subscripts L and R denote the left and right-side face contributions, and \mathcal{M}_4^\pm and \mathcal{P}_5^\pm are the Mach number interpolation functions. In a previous paper, dealing with pure fluid flow without magnetic interaction [26], we described a method that use these interpolation functions to obtain cell face values of velocity and pressure, and a PISO-type algorithm was then applied to the Euler equations at arbitrary Mach numbers. The purpose here is to devise a similar method of assembling the fluxes for the MHD system of equations.

The AUSM method was developed specifically for gas dynamics, using the appropriate characteristic speeds, and it is not readily applicable to MHD flow. The main issue is that the ideal MHD equations have seven different characteristic speeds, instead of three as in Euler equations. So, to properly scale the Mach number interpolation functions, we adapted to our method the weighting functions of Han *et al.* [18], which take into account the magnetic field. The scaled \mathcal{M}_4^\pm are then given by the following:

$$\begin{aligned} M_f = \mathcal{M}_4^+ + \mathcal{M}_4^- \geq 0: \\ \bar{\mathcal{M}}_4^- = \mathcal{M}_4^- \cdot w \cdot (1 + f_R), \\ \bar{\mathcal{M}}_4^+ = \mathcal{M}_4^+ + \mathcal{M}_4^- \cdot [(1 - w) \cdot (1 + f_R) - f_L], \end{aligned} \quad (13)$$

$$\begin{aligned} M_f = \mathcal{M}_4^+ + \mathcal{M}_4^- < 0: \\ \bar{\mathcal{M}}_4^+ = \mathcal{M}_4^+ \cdot w \cdot (1 + f_L), \\ \bar{\mathcal{M}}_4^- = \mathcal{M}_4^- + \mathcal{M}_4^+ \cdot [(1 - w) \cdot (1 + f_L) - f_R], \end{aligned} \quad (14)$$

where f and w are functions of the global pressure defined by the following:

$$f_{L,R} = \begin{cases} \left(\frac{p_{G,L} + p_{G,R}}{p_{G,s}} - 1 \right), & p_{G,s} \neq 0 \\ 0, & p_{G,s} = 0 \end{cases}, \quad p_{G,s} = \mathcal{P}_5^+ p_{G,L} + \mathcal{P}_5^- p_{G,R}, \quad (15)$$

$$w = 1 - \min \left(\frac{p_{G,L}}{p_{G,R}}, \frac{p_{G,R}}{p_{G,L}} \right)^3, \quad (16)$$

with

$$p_{G,L} = p_L + \frac{1}{2} (B_x^2 + B_y^2 + B_z^2)_L, \quad (17)$$

$$p_{G,R} = p_R + \frac{1}{2} (B_x^2 + B_y^2 + B_z^2)_R. \quad (18)$$

In addition, the interface Mach number needs to be calculated with the fast magnetosonic speed, and not with the standard sound speed as in the AUSM⁺ method. That is, the left and right states of the Mach number become the following:

$$M_{L,R} = \frac{U_{L,R}}{c_f}, \quad (19)$$

with the common magnetosonic fast speed at the cell face calculated as follows:

$$c_f = \min(c_{f,L}, c_{f,R}), \quad (20)$$

$$c_{f,L} = \left\{ \frac{1}{2} \left[a_L^2 + \frac{B_L^2}{\rho_L} + \sqrt{\left(a_L^2 + \frac{B_L^2}{\rho_L} \right) - 4a_L^2 \frac{B_{n,L}^2}{\rho_L}} \right] \right\}^{\frac{1}{2}}, \quad (21)$$

$$c_{f,R} = \left\{ \frac{1}{2} \left[a_R^2 + \frac{B_R^2}{\rho_R} + \sqrt{\left(a_R^2 + \frac{B_R^2}{\rho_R} \right) - 4a_R^2 \frac{B_{n,R}^2}{\rho_R}} \right] \right\}^{\frac{1}{2}}, \quad (22)$$

where $a_{L,R}$ are the left and right states of the speed of sound at the cell interface, and $B_n = \hat{\mathbf{S}}_f \cdot \mathbf{B}$ is the normal component of the magnetic field.

3.2. Treatment of the $\nabla \cdot \mathbf{B} = 0$ constraint

In multidimensional MHD flow simulations, special care needs to be taken to ensure that the $\nabla \cdot \mathbf{B} = 0$ constraint is satisfied or, at least, that its value is small. It has been demonstrated by Brackbill and Barnes [22] that, even if the solenoidal condition is satisfied at the initial time step, numerical errors related to time and space discretization are magnified, as a result of the following evolution equation for $\nabla \cdot \mathbf{B}$:

$$\frac{\partial}{\partial t} (\nabla \cdot \mathbf{B}) = 0 + \mathcal{O}(\Delta x^m, \Delta t^n), \quad (23)$$

with $m, n \geq 1$. To handle this problem, we apply the hyperbolic/parabolic divergence cleaning method suggested by Dedner *et al.* [25]. Their proposal was to couple the $\nabla \cdot \mathbf{B} = 0$ constraint to the evolution equation for \mathbf{B} by means of a scalar function Ψ , through a gradient term,

$$\frac{\partial \mathbf{B}}{\partial t} + \nabla \cdot (\mathbf{UB} - \mathbf{BU}) + \nabla \Psi = 0. \quad (24)$$

So, an additional equation needs to be assembled and solved for this scalar Ψ ; in our case, we have implemented the following hyperbolic/parabolic equation:

$$\frac{\partial \Psi}{\partial t} + c_h^2 \nabla \cdot \mathbf{B} = -\frac{c_h^2}{c_d^2} \Psi. \quad (25)$$

This equation implies that the errors associated to $\nabla \cdot \mathbf{B}$ are convected by the c_h speed and, at the same time, are damped by the dissipation coefficient c_d . The c_h speed is determined by the following:

$$c_h = \frac{CFL}{\Delta t \times \max(\frac{1}{d})}, \quad (26)$$

$$CFL = \max \left[\frac{(|U_f| + c_f) \Delta t}{d} \right], \quad (27)$$

where d is the cell size and $U_f = c_f (\bar{\mathcal{M}}_4^+ + \bar{\mathcal{M}}_4^-)$ is the cell face velocity. With this approach, c_h is the maximum speed that is compatible with the CFL number. The dissipation coefficient is given by the following:

$$c_d = \sqrt{-\Delta t \frac{c_h^2}{\ln(c_r)}}, \text{ with } 0 < c_r < 1, \quad (28)$$

and in all calculations, we set $c_r = 0.9$.

3.3. Description of the algorithm

The algorithm proposed is based on the PISO method of Issa [27]. In a previous paper [26], we described the first version of the algorithm that was then applied to solve the Euler equations at arbitrary Mach numbers. In the present work, we explain the steps required to extend that algorithm to the solution of the ideal MHD equations. A segregated approach is followed consisting of successive prediction and correction steps, with values obtained at a previous time step denoted with n , and consecutive predictions and corrections denoted with $*$, $**$, $***$.

3.3.1. Prediction step. In this first step, all nodal values are assumed to be known at the previous time level n . The interpolation Mach number functions are calculated at the beginning of each time step using Equations (13) and (14). With these functions, we calculate the fluxes for the following 3-D MHD equations:

$$\mathcal{F}_f = c_f (\bar{\mathcal{M}}_4^+ \Phi_L^n + \bar{\mathcal{M}}_4^- \Phi_R^n) + (\mathcal{P}_5^+ \mathbf{P}_L^n + \mathcal{P}_5^- \mathbf{P}_R^n) + \frac{1}{2} (\Phi_{\mathbf{B},L}^n + \Phi_{\mathbf{B},R}^n), \quad (29)$$

$$\Phi = \begin{pmatrix} \rho \\ \rho U_x \\ \rho U_y \\ \rho U_z \\ B_x \\ B_y \\ B_z \\ \rho e + p_G \\ 0 \end{pmatrix}, \quad \mathbf{P} = \begin{pmatrix} 0 \\ S_x p_G \\ S_y p_G \\ S_z p_G \\ -\bar{B}_f U_x \\ -\bar{B}_f U_y \\ -\bar{B}_f U_z \\ -\bar{B}_f (\mathbf{U} \cdot \mathbf{B}) \\ 0 \end{pmatrix}, \quad \Phi_{\mathbf{B}} = \begin{pmatrix} 0 \\ -B_x \bar{B}_f \\ -B_y \bar{B}_f \\ -B_z \bar{B}_f \\ S_x \Psi \\ S_y \Psi \\ S_z \Psi \\ 0 \\ c_h^2 B_f \end{pmatrix}. \quad (30)$$

Here, $B_f = S_x B_x + S_y B_y + S_z B_z$, with S_x , S_y , and S_z being the cell face area components, and $\bar{B}_f = (B_{f,L} + B_{f,R})/2$; see [18] for more details. Because we are using PISO as the base pressure/velocity algorithm, we need to remove the magnetic pressure from the global pressure. In this way, we can obtain the face value of the thermodynamic pressure, which is required in the pressure gradient term of the following momentum equation (see [26]):

$$p_f^n = \mathcal{P}_5^+ p_L^n + \mathcal{P}_5^- p_R^n. \quad (31)$$

The first equation to be solved is an explicit version of the continuity equation, on the basis of the mass flux m_f that was previously assembled with the AUSM-MHD method (Equations (29) and (30), first line). The solution of this equation gives us a predicted value of density,

$$\frac{\partial \rho^*}{\partial t} + \nabla \cdot (m_f^n) = 0, \quad (32)$$

$$m_f^n = c_f^n (\bar{\mathcal{M}}_4^+ \rho_L^n + \bar{\mathcal{M}}_4^- \rho_R^n). \quad (33)$$

After this, an explicit equation for each component of the magnetic field is solved,

$$\frac{\partial B_i^*}{\partial t} + \nabla \cdot (\mathcal{B}_f^n) = 0, \quad (34)$$

$$\begin{aligned} \mathcal{B}_f^n = & c_f^n (\bar{\mathcal{M}}_4^+ B_{i,L}^n + \bar{\mathcal{M}}_4^- B_{i,R}^n) - \left(\mathcal{P}_5^+ [(\bar{B}_f)^n U_i^n]_L + \mathcal{P}_5^- [(\bar{B}_f)^n U_i^n]_R \right) \\ & + \frac{1}{2} ([S_i \Psi^n]_L + [S_i \Psi^n]_R), \end{aligned} \quad (35)$$

where the subscript i represents the multiple components of vector \mathbf{B} ($i = x, y, z$). For 1-D flows, with variations along the x -axis, to satisfy the $\nabla \cdot \mathbf{B} = 0$ condition, we must impose $B_x = \text{const.}$ To obey this condition, we neglect the B_x equation and just solve for B_y and B_z . Equation (34) is based on fluxes that were calculated previously with the AUSM-MHD method (Equation (35)) and their solution give predicted values of B_x^* , B_y^* , and B_z^* .

Predicted values of the velocity field, \mathbf{U}^* , at the present time step are obtained by solving explicit momentum equations for each direction,

$$\frac{\partial (\rho^* U_i^*)}{\partial t} + \nabla \cdot (\mathcal{U}_f^n) = -\nabla p_f^n, \quad (36)$$

$$\begin{aligned} \mathcal{U}_f^n = & c_f^n (\bar{\mathcal{M}}_4^+ [\rho_L^* U_{i,L}^n] + \bar{\mathcal{M}}_4^- [\rho_R^* U_{i,R}^n]) + \left(\mathcal{P}_5^+ \left[S_i \frac{(B^*)^2}{2} \right]_L + \mathcal{P}_5^- \left[S_i \frac{(B^*)^2}{2} \right]_R \right) \\ & - \frac{1}{2} ([(\bar{B}_f)^n B_i^*]_L + [(\bar{B}_f)^n B_i^*]_R). \end{aligned} \quad (37)$$

The pressure gradient and the magnetic field terms are treated in an explicit way using the predicted magnetic field values B_x^* , B_y^* , B_z^* (from Equation (34)), and the face values of pressure are calculated with Equation (31). The discretized momentum equation for \mathbf{U}^* is given by,

$$a_P^U \mathbf{U}^* = \mathbf{H}(\mathbf{U}^n) - \nabla p_f^n, \quad (38)$$

where a_P^U is the central velocity coefficient and the operator $\mathbf{H}(\mathbf{U}^n)$ is built using the convective terms of neighbor cells to P , the magnetic explicit terms, and the explicit part of the time derivative as follows:

$$\mathbf{H}(\mathbf{U}^n) = \sum a_N^U \mathbf{U}_N^n + S_B^* + \frac{\mathbf{U}^n}{\Delta t}. \quad (39)$$

The last equation to be solved, before the PISO correction cycle, is an equation for the total energy,

$$\frac{\partial (\rho^* e^*)}{\partial t} + \nabla \cdot (\mathcal{E}_f^n) = 0, \quad (40)$$

$$\begin{aligned} \mathcal{E}_f^n = & c_f^n \left(\bar{\mathcal{M}}_4^+ \left[\rho_L^* e_L^n + \frac{(B^*)^2_L}{2} + p_L^n \right] + \bar{\mathcal{M}}_4^- \left[\rho_R^* e_R^n + \frac{(B^*)^2_R}{2} + p_R^n \right] \right) \\ & - (\mathcal{P}_5^+ [(\bar{B}_f)^n (\mathbf{U}^* \cdot \mathbf{B}^*)]_L + \mathcal{P}_5^- [(\bar{B}_f)^n (\mathbf{U}^* \cdot \mathbf{B}^*)]_R), \end{aligned} \quad (41)$$

followed by a temperature, T , update using the equation of state,

$$T^* = \frac{1}{c_v} \left[e^* - \frac{1}{2} \left\{ (U^*)^2 + \frac{(B^*)^2}{\rho^*} \right\} \right]. \quad (42)$$

With this, this new temperature, new values of the compressibility coefficient are evaluated, $\psi^* = 1/RT^*$, and density is updated, $\rho^{**} = \psi^* p^n$.

3.3.2. Correction step. The $\mathbf{H}(\mathbf{U}^n)$ operator gives an intermediate velocity field that does not take into account the effect of pressure (see [26] for more details). Mach number interpolation functions are calculated once again inside the PISO cycle, with the AUSM-MHD method. These new functions serve to calculate the sonic flux to be used in the pressure equation,

$$F_s^* = c_f^* (\bar{\mathcal{M}}_4^+ \psi_L^* + \bar{\mathcal{M}}_4^- \psi_R^*). \quad (43)$$

This pressure equation is built and solved using the previously obtained values for compressibility, ψ^* , and density, ρ^{**} , as follows:

$$\frac{\partial(\psi^* p^*)}{\partial t} + \nabla \cdot (F_s^* p^*) - \nabla \cdot \left(\frac{\rho^{**}}{a_p^U} \nabla p^* \right) = 0, \quad (44)$$

and gives the predicted value for the pressure, p^* . The velocity field is corrected in an explicit way using the new pressure gradient and the first predicted velocity. The pressure gradient is again calculated with the pressure face value calculated using interpolated Mach number functions,

$$\mathbf{U}^{**} = \frac{\mathbf{H}(\mathbf{U}^n) - \nabla p_f^*}{a_p^U}. \quad (45)$$

Finally, density is corrected again using the equation of state $\rho^{***} = \psi^* p^*$. This cycle should be repeated until the continuity equation is satisfied, and in all calculations, we have used two correction steps.

4. TEST CASES

In the following subsections, we present some of the test cases used for validation. First, we calculate the circularly polarized Alfvén waves using 1-D and 2-D formulations. With this test case, we intend to validate our solver for smooth flows. Then, we consider several MHD cases with discontinuities in both the velocity and the magnetic fields. For that purpose, the rotated 1-D Riemann problem, the Orszag–Tang vortex problem, and the low- β cylinder are computed.

4.1. Circularly polarized Alfvén waves

The first set of test cases allows us to validate the accuracy of our method for smooth flows. These test cases are standard problems for MHD schemes [23, 28], and they offer analytical solutions of the MHD equations for arbitrary amplitudes. They can be calculated using a 1-D formulation of the MHD equations in a 1-D grid. But it is also possible to rotate the geometry at an angle α with respect to the x -axis, and in this case, the problem requires a 2-D solution.

The boundary conditions are periodic with $x \in [0; 1]$ for the 1-D case, and with $(x, y) = [0; 1/\cos \alpha] \times [0; 1/\sin \alpha]$ for the 2-D case. The initial conditions are the following: $\rho = 1$; $\gamma = 5/3$; $U_{\parallel} = 0$; $B_{\parallel} = 0$; $U_{\perp} = B_{\perp} = 0.1 \sin[2\pi(x \cos \alpha + y \sin \alpha)]$; $U_z = B_z = 0.1 \cos[2\pi(x \cos \alpha + y \sin \alpha)]$.

The Alfvén speed is $|U_A| = B_{\parallel}/\sqrt{\rho} = 1$, and, in this case, at $t = 1[s]$, the flow is expected to return to its initial state. The x and y components of the magnetic field are given by the following: $B_x = B_{\parallel} \cos \alpha - B_{\perp} \sin \alpha$; and $B_y = B_{\parallel} \sin \alpha + B_{\perp} \cos \alpha$ (similarly for velocity). As expected, for 1-D flow, $B_x = B_{\parallel}$ and $B_y = B_{\perp}$.

In Figure 1, we present the results obtained for the magnetic field components. These are for the 1-D case ($\alpha = 0$) with grid resolutions of $N = 128$, $N = 64$, $N = 32$, and $N = 16$, and the profiles of the B_y and B_z magnetic components are shown after five periods. We see that regarding the wave amplitude, even the lower grid resolution results agree well with the initial reference solution, which was obtained with the finer grid. If we compare these same results with those obtained using density-based solvers described in literature (see, for example, the results obtained by Tóth [23]), then we can see that, for a low grid resolution, the wave damping is generally quite severe, a feature that is absent in our case. However, our results do present a small phase error that is almost completely removed when the grid resolution is increased.

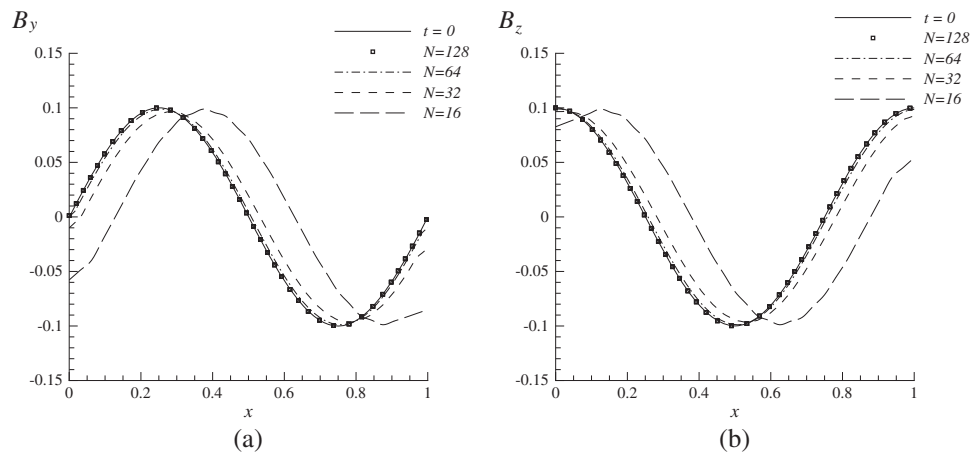


Figure 1. Results obtained for the B_y and B_z components of the magnetic field, calculated with three different grid resolutions. The continuous line shows the initial distribution calculated on the $N = 128$ grid.

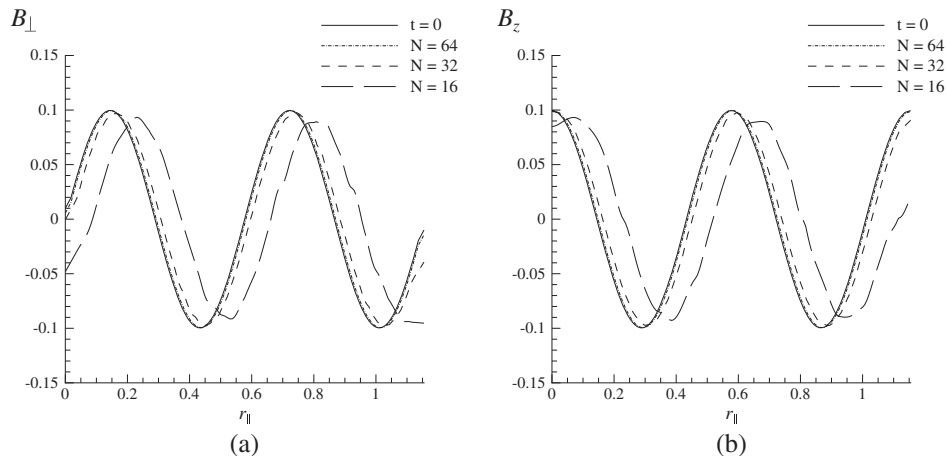


Figure 2. Results obtained for the perpendicular, B_{\perp} , and the B_z components of the magnetic field after five periods projected against a vector parallel to direction of wave propagation. The full line shows the initial distribution calculated on the $N = 64$ grid.

The second test is the corresponding 2-D case, which is solved on a $N \times N$ grid making an angle $\alpha = 30^\circ$ with the x -axis. We have performed this test with three successive grid resolutions: $N = 64$, $N = 32$, and $N = 16$. In Figure 2, we present the results for the perpendicular ($B_{\perp} = B_y \cos \alpha - B_x \sin \alpha$) and z -components of the magnetic field vector projected against a vector parallel to the direction of the wave propagation $r_{\parallel} = x \cos \alpha + y \sin \alpha$. We plot the solution obtained after five periods using the three grid resolutions, and for comparison, we also show the initial solution on the finest $N = 64$ grid. This figure demonstrates that, on the finest grid, the magnetic field returns to its initial state, as expected. We can see that the wave amplitude is again maintained. Although more tests are needed, these results are a good indicator that the all Mach pressure-based solver, presented here for the MHD equations, is fulfilling its purpose.

To verify that the proposed algorithm achieves second-order convergence in space, we performed a grid convergence study for the 1-D and 2-D cases. In both cases, four different grid resolutions were used: $N = 16$, $N = 32$, $N = 64$, and $N = 128$. The order of accuracy of the method was

estimated using the average of the relative error for the perpendicular component of the magnetic field calculated with the \mathcal{L}_2 norm:

$$\|e_h\|_{\mathcal{L}_2} = \frac{1}{n} \sum_{i=1}^n \sqrt{\frac{(B_i - B_{i,0})^2}{B_{i,0}^2}}, \quad (46)$$

were $B_{i,0}$ is the value obtained with the finest grid for the perpendicular component of \mathbf{B} at the initial time level, and n represents the number of points that were used in the average calculation. In Figure 3, we present the plots for the relative errors calculated with the \mathcal{L}_2 norm on a log-log scale, where the cell spacing is given by either $h = 1/N$ for the 1-D case, or $1/\cos\alpha/N$ for the 2-D case. For comparison, we also plot the second-order slope. We can observe that the relative errors in both plots decay in a second-order manner, as the grid is refined. This was expected because the Alfvén wave is a smooth test case without any discontinuities in the solution, and the formal order of the method should be retained by the numerical approximation. In the presence of discontinuities, it is expected that the actual order of convergence is reduced.

4.2. Rotated shock tube

In this section, we discuss the results for the 1-D Riemann problem in a 2-D perspective. In [23], it was shown that the 1-D shock tube problem can be converted to a 2-D problem using a $N \times 2$ grid if the discontinuous interface lies at an angle α to the y -axis. The computational domain is a narrow strip with $(x, y) = [0, 1] \times [0, 2/N]$, and the rotation angle is $\alpha \approx 63.4^\circ$. For the superior and inferior borders, we have imposed shifted periodic boundary conditions, and for the remaining borders, all variables were fixed, see Figure 4. All interpolations required relied on the high resolution Minmod limiter scheme.

Two different test cases were calculated. The first problem (*Case A*) is a 2.5-D solution of the rotated 1-D Riemann problem, and the second (*Case B*) test case is the classic Brio-Wu [12]

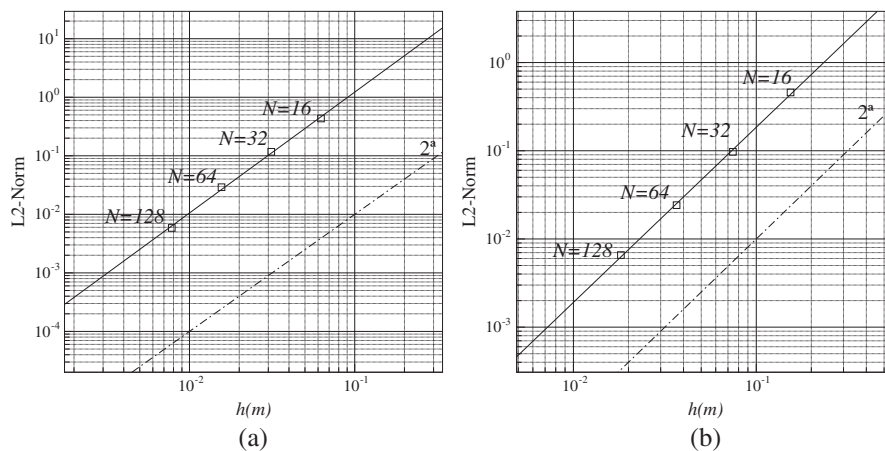


Figure 3. Spatial error obtained with the \mathcal{L}_2 norm as function of cell spacing h , for the perpendicular component of the magnetic field calculated (a) for the 1-D case and (b) for the 2-D case.

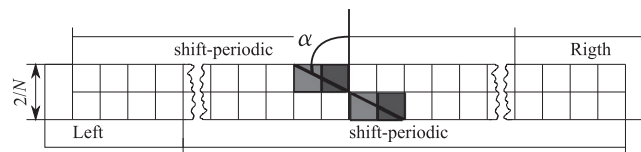


Figure 4. $N \times 2$ grid for the rotated shock tube problem. The periodic boundary conditions are shifted four cells in each direction.

shock tube, which is the MHD version of the gas dynamic Sod shock tube. The initial values for the left and right states are the following:

$$\text{Case A} \begin{pmatrix} \rho \\ U_{\parallel} \\ U_{\perp} \\ U_z \\ p \\ B_{\parallel} \\ B_{\perp} \\ B_z \end{pmatrix}_L = \begin{pmatrix} 1.08 \\ 1.2 \\ 0.01 \\ 0.05 \\ 0.95 \\ 2/\sqrt{4\pi} \\ 3.6/\sqrt{4\pi} \\ 2/\sqrt{4\pi} \end{pmatrix}, \quad \begin{pmatrix} \rho \\ U_{\parallel} \\ U_{\perp} \\ U_z \\ p \\ B_{\parallel} \\ B_{\perp} \\ B_z \end{pmatrix}_R = \begin{pmatrix} 1 \\ 0 \\ 0 \\ 0 \\ 1 \\ 2/\sqrt{4\pi} \\ 4/\sqrt{4\pi} \\ 2/\sqrt{4\pi} \end{pmatrix}. \quad (47)$$

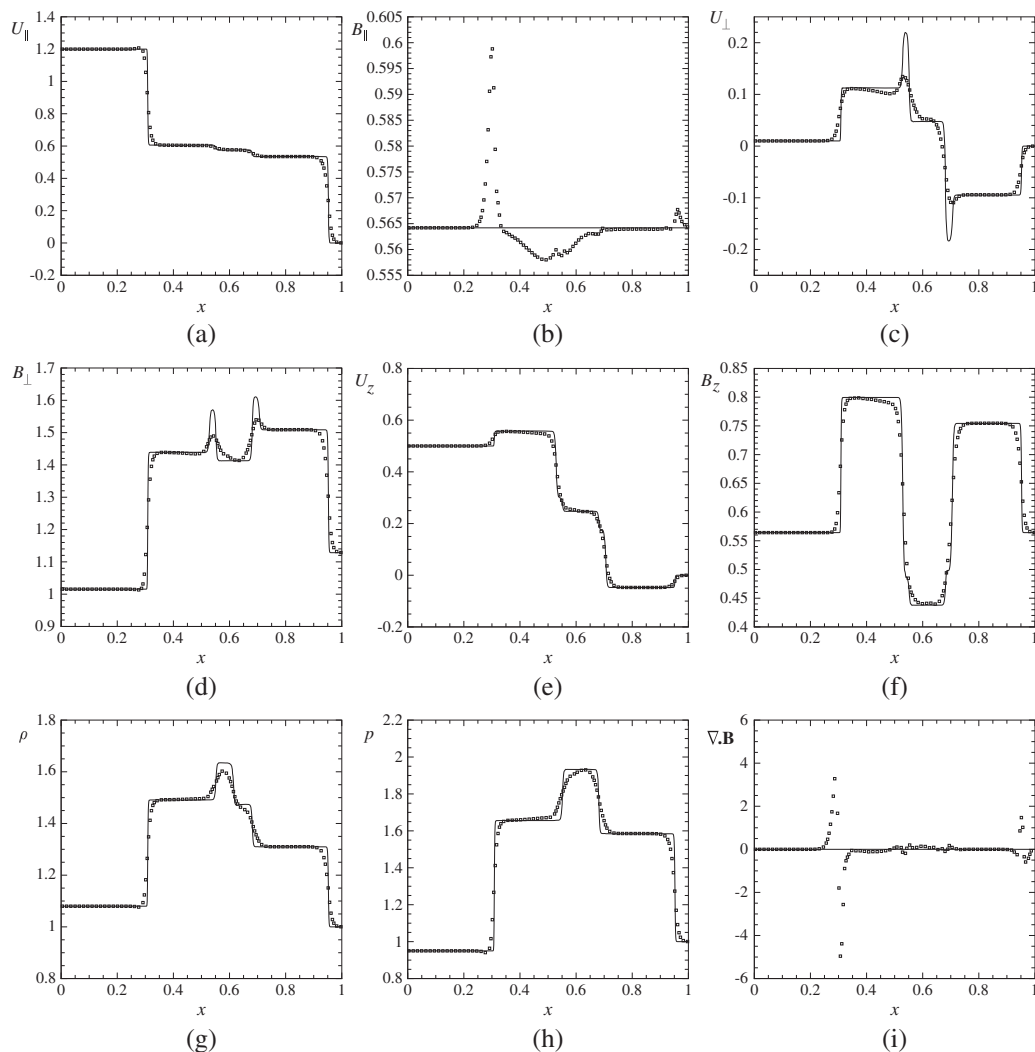


Figure 5. Results for the 2.5-D solution of the rotated Riemann problem (square symbols), compared with a 1-D reference solution calculated on an $N = 1024$ grid (lines). The various plots show the following: the perpendicular, the parallel ($B_{\parallel} = B_x \cos \alpha + B_y \sin \alpha$, with the same for velocity) and (a, c, and e) the z components of velocity and (b, d, and f) magnetic fields; density; pressure; and divergence of \mathbf{B} .

$$\text{Case B} \begin{pmatrix} \rho \\ U_{\parallel} \\ U_{\perp} \\ U_z \\ p \\ B_{\parallel} \\ B_{\perp} \\ B_z \end{pmatrix}_L = \begin{pmatrix} 1 \\ 0 \\ 0 \\ 0 \\ 1 \\ 0.75 \\ 1/\sqrt{4\pi} \\ 0 \end{pmatrix}, \quad \begin{pmatrix} \rho \\ U_{\parallel} \\ U_{\perp} \\ U_z \\ p \\ B_{\parallel} \\ B_{\perp} \\ B_z \end{pmatrix}_R = \begin{pmatrix} 0.125 \\ 0 \\ 0 \\ 0 \\ 0.1 \\ 0.75 \\ -1 \\ 0 \end{pmatrix}. \quad (48)$$

For the adiabatic index, we have used $\gamma = 5/3$.

In Figure 5, we present results obtained for the *Case A* at $t = 0.2 \cos \alpha$, and in Figure 6, we present the results for the *Case B* at $t = 0.1 \cos \alpha$. Both sets of plots show results for the 2-D solution

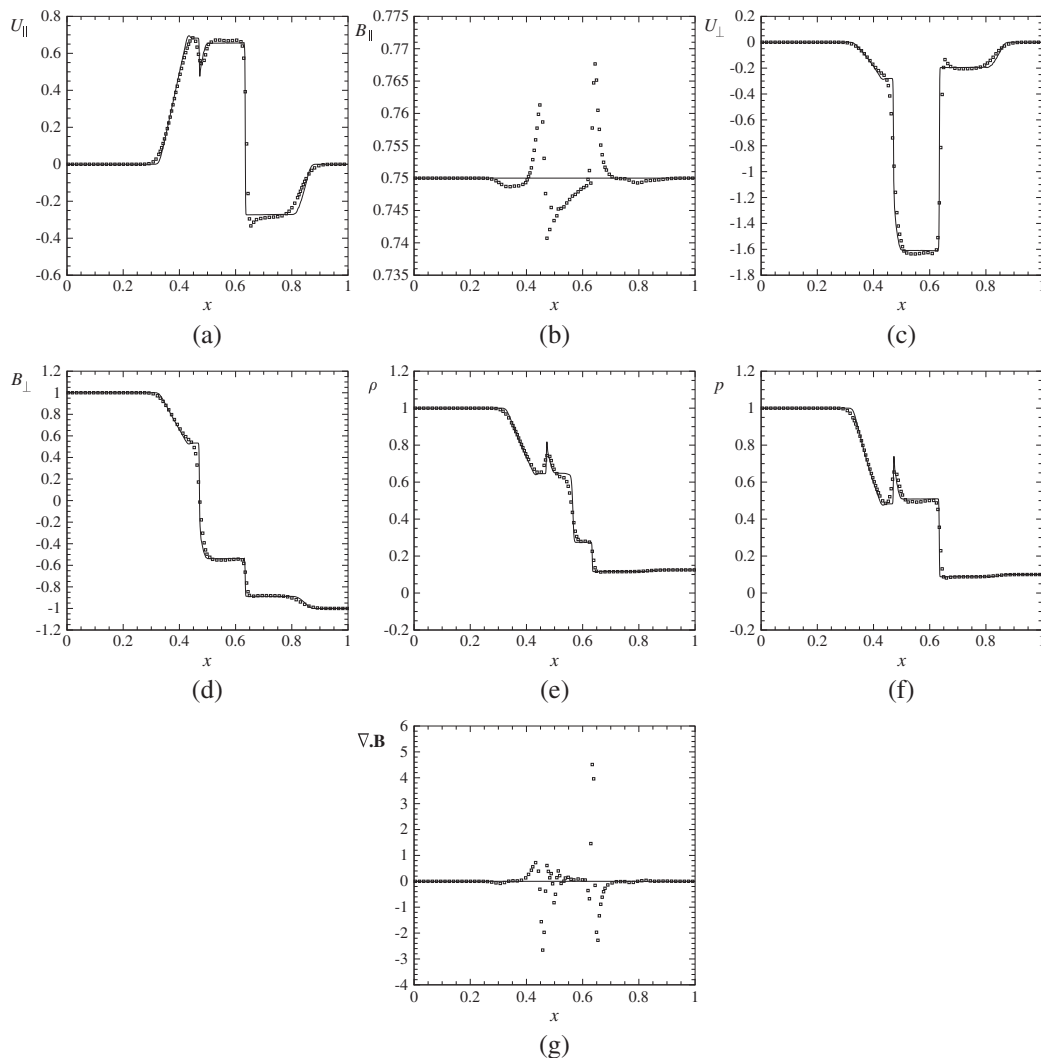


Figure 6. 2-D Results for the Brion-Wu solution of the rotated Riemann problem (square symbols), compared with a 1-D reference solution calculated on an $N = 1024$ grid (lines). The plots show the following: (a and c) the perpendicular and parallel components of velocity, and (b and d) magnetic fields; (e) density; (f) pressure; and (g) divergence of \mathbf{B} .

compared with a high resolution 1-D solution ($N = 1024$). It is clear that the 2-D results look somewhat more diffused when compared with the 1-D reference solution for this $N = 256$ grid resolution. This feature can be explained because, as noticed by Tóth [23], using an $N \times 2$ grid approach to mimic a 2-D situation give an effective resolution three times lower than that on an $N \times N$ grid for the same value of N . Nevertheless, such a procedure turns out to be more economical, and it is possible to check that our 2-D results capture the correct physics of the problem. In *Case A*, flow features from left to right (Figure 5): fast shock; rotational discontinuity; slow shock; contact discontinuity; slow shock; rotational discontinuity; and fast shock. In *Case B*, the flow exhibits the following discontinuities, also from left to right (Figure 6): fast rarefaction; slow compound; contact discontinuity; slow shock; and fast rarefaction. We notice that the divergence of \mathbf{B} only exhibits clear nonzero values close to the discontinuities in the perpendicular component of \mathbf{B} , thus supporting the present treatment of that constraint.

4.3. Orszag–Tang vortex

The third test case is the Orszag–Tang vortex, which is a well-known 2-D test case for MHD schemes [6, 13, 23, 28]. Starting from smooth initial conditions, this test case leads to a system of complex MHD shocks, making this problem an ideal test for assessing the ability of the method to handle the complex interaction of several MHD discontinuities included in the evolution of the vortex. The computational domain is a square box with $(x, y) = [0; 2\pi] \times [0; 2\pi]$, and periodic boundary conditions are applied everywhere. The initial conditions are given by the following: $\rho = \gamma^2$; $U_x = -\sin y$; $U_y = \sin x$; $U_z = 0$; $B_x = -\sin y$; $B_y = \sin 2x$; $B_z = 0$; $p = \gamma$; $\gamma = 5/3$. In this case, the CUBISTA [29] scheme was used for variable interpolation. This interpolation scheme is very robust and accurate in the calculation of discontinuities, however, when applied with the AUSM schemes in the presence of very strong shock regions becomes too much compressive and produces some overshoots; we prefer then to use more dissipative schemes like the Minmod limiter applied in Section 4.2. This particular issue was also noticed by different authors, for example, [19]. The present problem was calculated on an $N \times N$ grid using three different resolutions ($N = 200$, $N = 400$, and $N = 800$).

In Figure 7(a), (b), and (c), we present the predicted results in terms of pressure contour lines calculated at $t = \pi$ on the three grids. Careful inspection of these plots allows us to infer that the MHD shock interaction is calculated with accuracy for all values of N . Additional more quantitative comparison requires data from other sources. In this case, we have chosen to compare our results with those obtained by Miyoshi and Kusano [6]. These authors provide suitable data for comparison because their choices for length and time units were the same as ours, and in addition, their method was very efficient and accurate for the computation of ideal MHD equations. Such comparison is presented in Figure 7(d) that show the pressure distribution along the line $y = 0.64\pi$. We see that our method performs well, and the data of [6] is replicated with accuracy, although some discrepancies are observed in the initial part of this particular pressure profile. Miyoshi and Kusano did mention that more dissipative schemes tend to give such type of discrepancy, which are more noticeable in the two larger discontinuities, where the Roe scheme used by those authors seems to present sharper shock wave resolution.

4.4. Low- β plasma flow over a perfectly conducting cylinder

The gas dynamic version of this test case was already computed with our previous pure Euler method, see [26] for more details. Here, we intend to study the MHD version, for a low- β perfectly conductor plasma, over a perfectly conducting cylinder. This case has a physical meaning because it can be seen as a 2-D version of the interaction between solar winds with a magnetosphere. The plasma parameter $\beta = 2p/B^2$ relates pure gas dynamic and magnetic forces; namely, for $\beta \gg 1$, the pure gas dynamic forces (namely, the pressure) govern the flow, and for $\beta \ll 1$, the flow is controlled by magnetic forces.

This test case was extensively tested by Sterck *et al.* [30], who have discussed all possible types of discontinuities that can arise from the MHD equations. Using a pure analytical approach,

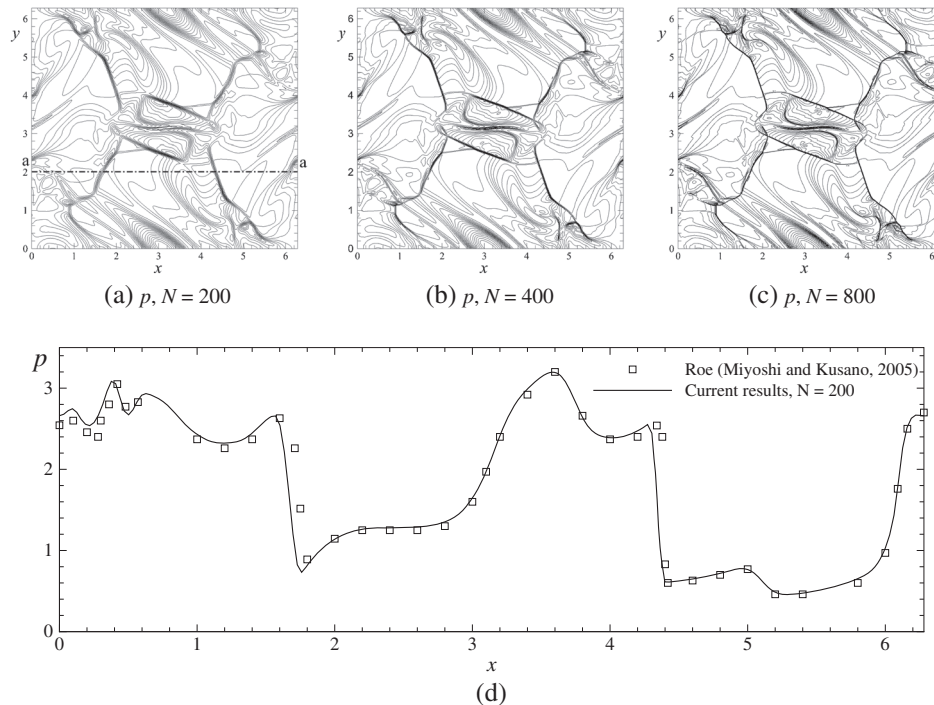


Figure 7. Numerical results for the Orszag–Tang vortex at $t = \pi$. Pressure contour lines calculated on grids with: (a) $N = 200$; (b) $N = 400$; (c) $N = 800$. (d) Comparison between current predictions and results by Miyoshi and Kusano [6] with a Roe-type solver, for the section a-a defined in (a).

they have also proved that the intermediate shocks, which can be generated by this case, have a physical meaning.

Regarding the solution domain, we have a similar mesh as in [26]. The flow was only computed on the upper left quadrant for three grid resolutions successively refined: 120×120 , 240×240 , and 480×480 . The structured grid is stretched, elliptic polar-like, extending from $x = 0$ to $x = -0.35$ in the x -axis, and from $y = 0$ to $y = 1.4$ in the y -axis. This case has a steady state solution that is uniquely determined for given inlet plasma parameter β and inlet Alfvén Mach number, see [30]. The initial flow, incoming from the left, is aligned with the magnetic field and faces a perfectly conducting circular obstacle. We have used the same values for the parameters as Sterck *et al.*: for the plasma beta, $\beta = 0.4$; and for the Alfvén Mach number, $M_{\text{Alfvén}} = 1.5$. To obtain those values, the relevant physical properties were the following, at inlet: $\rho = 1$, $B_x = 1$, $p = 0.2$ e $U_x = 1.5$. We have imposed typical supersonic boundary conditions, with, at inlet, all variables being specified and, at the outlet, all variables being extrapolated from the interior of the solution domain. In this test case, because of the strong shock wave region, we have used the Minmod limiter for variable interpolation.

In Figure 8(a), (b), and (c), we present the Mach number contour lines calculated with the three grids resolutions. The bottom Figure 8(d), (e), and (f) show a detail of the results near the cylinder wall, with the same contour plots and including the magnetic field lines. Using these lines and the discontinuities as guide, we can actually point each one of the possible MHD shocks that may arise in this particular problem. We can see intermediate shocks when the direction of B_y changes in the downstream region to the shock wave. Other types of MHD shocks that may be identified from such plots are the fast switch-on shocks and the slow switch-off shocks. In the fast switch-on shocks, the B_y component vanishes in upstream region of the discontinuity and $B_y \neq 0$ in the downstream region, so the tangential component of \mathbf{B} is switch-on. In contrast, in the slow switch-off shocks, B_y vanishes in the region downstream of the discontinuity. We can see that, once again, our method can calculate those MHD discontinuities with a good level of accuracy.

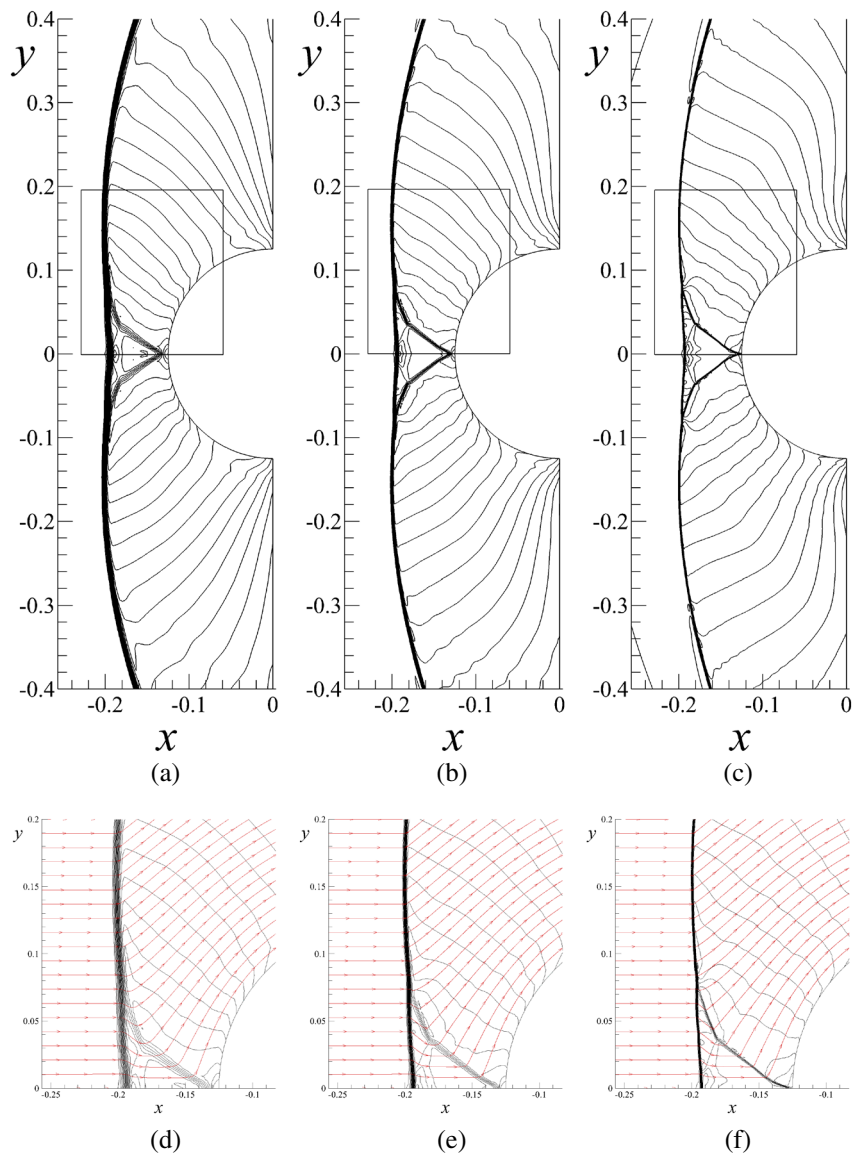


Figure 8. Mach number results obtained for the cylinder flow using the three grid resolutions: (a and d) 120×120 ; (b and e) 240×240 ; and (c and f) 480×480 . Plots (d), (e), and (f) show a detail of the solution including magnetic field lines, as they interact with the discontinuities.

5. CONCLUSION

In the current paper, we have presented in some detail a pressure-based method for the solution of the ideal MHD equations and have discussed the results obtained when the method is applied to several cases. The test results for the Alfvén waves show a small phase error. However, we have proved that this new algorithm is more accurate in what regards the calculation of the wave amplitude, in particular when compared with density-based solvers currently found in the literature.

On the other hand, the results for the shock tube problem have clearly demonstrated that the new pressure-based algorithm can compute highly compressible MHD flow, including the complex discontinuities that are associated with this hyperbolic system of equations. The results for the Orszag–Tang vortex and the low- β cylinder problem have shown that the new formulation is able to capture the complex physics of shock wave interaction found in these representative MHD problems.

Further, regarding accuracy, the method proposed is shown to be competitive when compared with other solvers, which have proved to be highly accurate in the calculation of compressible MHD flows.

ACKNOWLEDGEMENTS

This work was supported by FCT grant SFRH/BD/60285/2009 and by FCT project PTDC/ CTESPA/114163/2009 'SpaceProp - MHD Numerical Modeling in nozzles of MPD Thrusters for Space Propulsion'. Additional financial support was provided by CAST.

REFERENCES

- Chanty J-MG. Analysis of two-dimensional flows in magneto-dynamic plasma accelerators. *PhD Thesis*, Massachusetts Institute of Technology, 1992.
- Ni M-J, Munipalli R, Morley NB, Huang P, Abdou MA. A current density conservative scheme for incompressible MHD flows at a low magnetic Reynolds number. Part I: on a rectangular collocated grid system. *Journal of Computational Physics* 2007; **227**(1):174–204. DOI: 10.1016/j.jcp.2007.07.023.
- Ryu D, Jones TW. Numerical magnetohydrodynamics in astrophysics: algorithm and tests for one-dimensional flow. *Astronomy and Astrophysics* March 1995; **442**:228–258. DOI: 10.1086/175437.
- Tóth G, Odstrčil D. Comparison of some flux corrected transport and total variation diminishing numerical schemes for hydrodynamic and magnetohydrodynamic problems. *Journal of Computational Physics* 1996; **128**(1):82–100. DOI: 10.1006/jcph.1996.0197.
- Li S. An HLLC Riemann solver for magneto-hydrodynamics. *Journal of Computational Physics* 2005; **203**(1):344–357. DOI: 10.1016/j.jcp.2004.08.020.
- Miyoshi T, Kusano K. A multi-state HLL approximate Riemann solver for ideal magnetohydrodynamics. *Journal of Computational Physics* 2005; **208**(1):315–344. DOI: 10.1016/j.jcp.2005.02.017.
- Balsara DS, Rumpf T, Dumbser M, Munz C-D. Efficient, high accuracy ADER-WENO schemes for hydrodynamics and divergence-free magnetohydrodynamics. *Journal of Computational Physics* 2009; **228**(7):2480–2516. DOI: 10.1016/j.jcp.2008.12.003.
- Takeda H, Yamamoto S. Numerical investigation of supersonic MPD viscous flows with ionization. *JSME International Journal Series B Fluids and Thermal Engineering* 2002; **45**(1):97–101. DOI: 10.1299/jsmeb.45.97.
- Evans CR, Hawley JF. Simulation of magnetohydrodynamic flows – a constrained transport method. *Astrophysical Journal* September 1988; **332**:659–677. DOI: 10.1086/166684.
- Stone JM, Norman ML. ZEUS-2D: a radiation magnetohydrodynamics code for astrophysical flows in two space dimensions. II. The magnetohydrodynamic algorithms and tests. *Astrophysical Journal Supplement* June 1992; **80**:791–818. DOI: 10.1086/191681.
- Falle SAEG. Rarefaction shocks, shock errors, and low order of accuracy in ZEUS. *The Astrophysical Journal Letters* 2002; **577**(2):L123. DOI: 10.1086/344336.
- Brio M, Wu CC. An upwind differencing scheme for the equations of ideal magnetohydrodynamics. *Journal of Computational Physics* 1988; **75**(2):400–422. DOI: 10.1016/0021-9991(88)90120-9.
- Zachary AL, Malagoli A, Colella P. A higher-order Godunov method for multidimensional ideal magnetohydrodynamics. *SIAM Journal on Scientific Computing* 1994; **15**(2):263–284. DOI: 10.1137/0915019.
- Janhunen P. A positive conservative method for magnetohydrodynamics based on HLL and Roe methods. *Journal of Computational Physics* 2000; **160**(2):649–661. DOI: 10.1006/jcph.2000.6479.
- Linde T. A practical, general-purpose, two-state HLL Riemann solver for hyperbolic conservation laws. *International Journal for Numerical Methods in Fluids* 2002; **40**(3-4):391–402. DOI: 10.1002/flid.312.
- Toro EF, Spruce M, Speares W. Restoration of the contact surface in the HLL-Riemann solver. *Shock Waves* 1994; **4**:25–34. DOI: 10.1007/BF01414629. 10.1007/BF01414629.
- Mignone A. A simple and accurate Riemann solver for isothermal MHD. *Journal of Computational Physics* 2007; **225**(2):1427–1441. DOI: 10.1016/j.jcp.2007.01.033.
- Han SH, Lee JI, Kim KH. Accurate and robust pressure weight advection upstream splitting method for magnetohydrodynamics equations. *AIAA Journal* April 2009; **47**:970–981. DOI: 10.2514/1.39375.
- Kim KH, Kim C, Rho O-H. Methods for the accurate computations of hypersonic flows: II. Shock-aligned grid technique. *Journal of Computational Physics* 2001; **174**(1):81–119. DOI: 10.1006/jcph.2001.6896.
- Kim KH, Kim C. Accurate, efficient and monotonic numerical methods for multi-dimensional compressible flows: Part I: Spatial discretization. *Journal of Computational Physics* 2005; **208**(2):527–569. DOI: 10.1016/j.jcp.2005.02.021.
- van der Heul DR, Vuik C, Wesseling P. A conservative pressure-correction method for the Euler and ideal MHD equations at all speeds. *International Journal for Numerical Methods in Fluids* 2002; **40**(3-4):521–529. DOI: 10.1002/flid.322.
- Brackbill JU, Barnes DC. The effect of nonzero $\nabla \cdot \mathbf{B}$ on the numerical solution of the magnetohydrodynamic equations. *Journal of Computational Physics* 1980; **35**(3):426–430. DOI: 10.1016/0021-9991(80)90079-0.
- Tóth G. The $\nabla \cdot \mathbf{B} = 0$ constraint in shock-capturing magnetohydrodynamics codes. *Journal of Computational Physics* July 2000; **161**:605–652. DOI: 10.1006/jcph.2000.6519.

24. Powell KG, Roe PL, Linde TJ, Gombosi TI, Zeeuw DLD. A solution-adaptive upwind scheme for ideal magnetohydrodynamics. *Journal of Computational Physics* 1999; **154**(2):284–309. DOI: 10.1006/jcph.1999.6299.
25. Dedner A, Kemm F, Kröner D, Munz C-D, Schnitzer T, Wesenberg M. Hyperbolic divergence cleaning for the MHD equations. *Journal of Computational Physics* 2002; **175**:645–673. DOI: 10.1006/jcph.2001.6961.
26. Xisto CM, Páscoa JC, Oliveira PJ, Nicolini DA. A hybrid pressure density-based algorithm for the Euler equations at all Mach number regimes. *International Journal for Numerical Methods in Fluids* 2012; **70**:961–976. DOI: 10.1002/fld.2722.
27. Issa RI. Solution of the implicitly discretized fluid flow equations by operator-splitting. *Journal of Computational Physics* 1986; **62**:40–65. DOI: 10.1016/0021-9991(86)90099-9.
28. Dai W, Woodward PR. A simple finite difference scheme for multidimensional magnetohydrodynamical equations. *Journal of Computational Physics* 1998; **142**(2):331–369. DOI: DOI:10.1006/jcph.1998.5944.
29. Alves MA, Oliveira PJ, Pinho FT. A convergent and universally bounded interpolation scheme for the treatment of advection. *International Journal for Numerical Methods in Fluids* 2003; **41**(1):47–75. DOI: 10.1002/fld.428.
30. Sterck HD, Low BC, Poedts S. Complex magnetohydrodynamic bow shock topology in field-aligned low-beta flow around a perfectly conducting cylinder. *Physics of Plasmas* 1998; **5**(11):4015–4027. DOI: 10.1063/1.873124.